Volume 52
Number 41
7 November 2023
Pages 14689-15134

Dalton Transactions

An international journal of inorganic chemistry

rsc.li/dalton

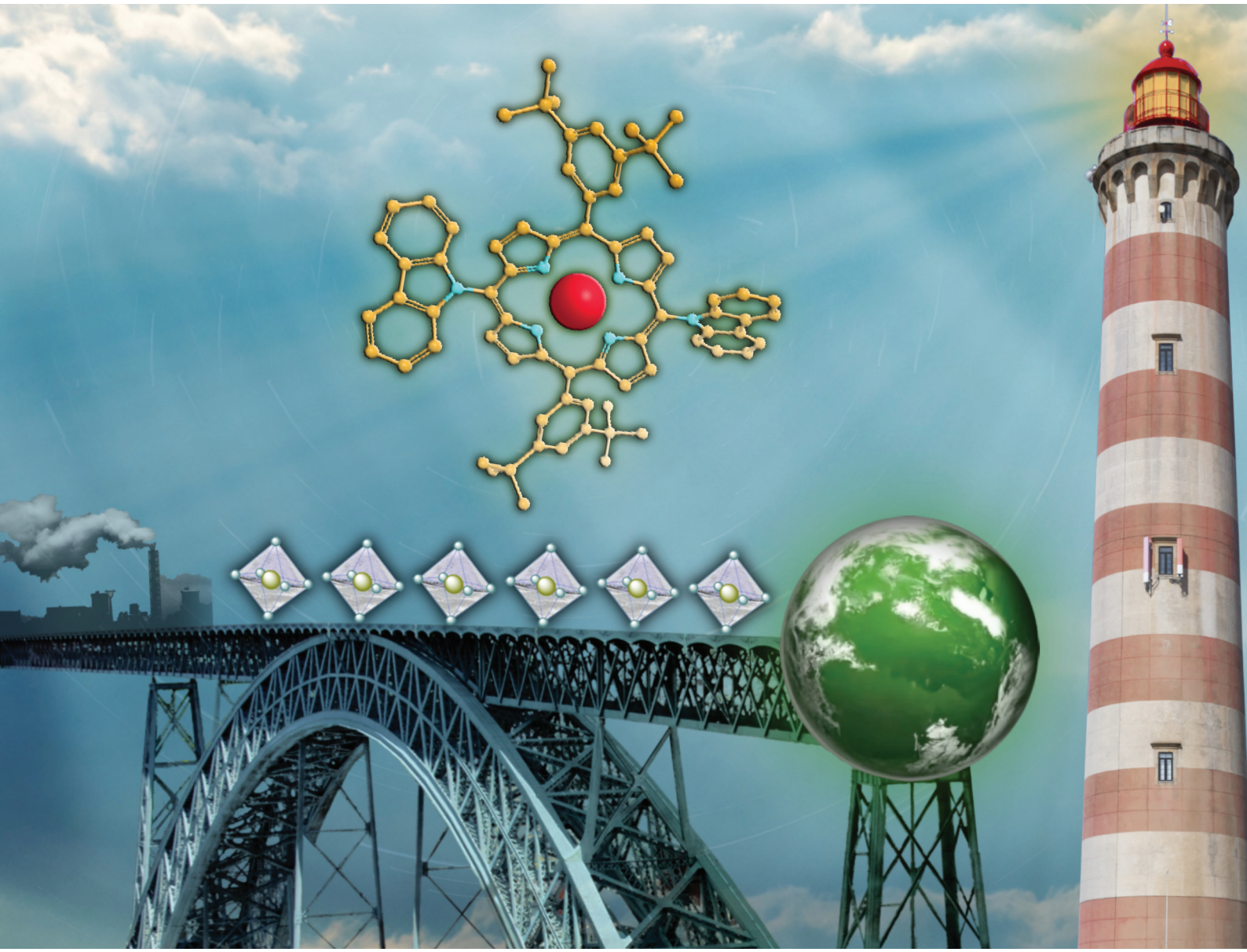

ISSN 1477-9226

ROYAL SOCIETY OF CHEMISTRY

PAPER

Nuno M. M. Moura, Ana M. V. M. Pereira *et al.*
C–N linked donor type porphyrin derivatives: unrevealed hole-transporting materials for efficient hybrid perovskite solar cells

Dalton Transactions

ROYAL SOCIETY OF CHEMISTRY

PAPER

View Article Online
View Journal | View Issue

Cite this: *Dalton Trans.*, 2023, **52**, 14762

C–N linked donor type porphyrin derivatives: unrevealed hole-transporting materials for efficient hybrid perovskite solar cells†

Melani J. A. Reis,‡[a] Ana T. Nogueira,‡[b,c] Ana Eulálio,[b,c] Nuno M. M. Moura, *[a] Joana Rodrigues,[d] Dzmitry Ivanou,[b,c] Paulo E. Abreu,[e] M. Rosário P. Correia,[d] Maria G. P. M. S. Neves,[a] Ana M. V. M. Pereira *[b,c] and Adélio Mendes[b,c]

A new series of Zn(II) and Cu(II)-based porphyrin complexes **5a** and **5b** doubly functionalised with carbazole units were developed to be used as hole-transporting materials (HTMs) in perovskite solar cells (PSCs). These complexes were obtained *via* a nucleophilic substitution reaction mediated by $PhI(OAc)_2$/$NaAuCl_4{\cdot}2H_2O$, or using C–N transition metal-assisted coupling. The hole extraction capability of **5a** and **5b** was assessed using cyclic voltammetry; this study confirmed the better alignment of the Zn(II) complex **5a** with the perovskite valence band level, compared to the Cu(II) complex **5b**. The optimised geometry and molecular orbitals of both complexes also corroborate the higher potential of **5a** as a HTM. Photoluminescence characterisation showed that the presence of **5a** and **5b** as HTMs on the perovskite surface resulted in the quenching of the emission, matching the hole transfer phenomenon. The photovoltaic performance was evaluated and compared with those of reference cells made with the standard HTM spiro-OMeTAD. The optimised **5**-based devices showed improvements in all photovoltaic characteristics; their open circuit voltage (V_{oc}) reached close to 1 V and short-circuit current density (J_{sc}) values were 13.79 and 9.14 mA cm^{-2} for **5a** and **5b**, respectively, disclosing the effect of the metallic centre. A maximum power conversion efficiency (PCE) of 10.01% was attained for **5a**, which is 65% of the PCE generated by using the spiro-OMeTAD reference. This study demonstrates that C–N linked donor-type porphyrin derivatives are promising novel HTMs for developing efficient and reproducible PSCs.

Received 17th February 2023,
Accepted 21st July 2023

DOI: 10.1039/d3dt00512g

rsc.li/dalton

1. Introduction

Nowadays, it is unquestionable that to meet the rapidly growing global energy demand and avoid large amounts of greenhouse gas emissions, renewable energy sources need to be exploited to the maximum extent. Indeed, solar power is the world's most abundant energy resource, and harnessing it would yield a never-ending energy supply.[1] Nonetheless, the greatest challenge has always been the development of efficient and cost-effective approaches to solar energy conversion. Photovoltaic (PV) technology is touted as the most promising pathway and the global PV market is currently being dominated by crystalline silicon solar cells, which have demonstrated a high power conversion efficiency (PCE) of 26.1%.[2] A cutting-edge breakthrough is now perovskite solar cells (PSCs).[3,4] The progress in this emerging technology is so impressive that from the first example reported in 2009 with a PCE of 3.8%,[5] the value increased to 12–16% by mid-2012 and 2013 and to a certified PCE of 26.0% in 2023.[2c] Most of these achievements are due to the presence of light absorbers based on lead perovskite materials, which exhibit broad absorption in the solar spectrum combined with high charge carrier mobility and low recombination. Even so, one of the most important technical improvements came from replacing the liquid redox mediator with a p-type solid-state hole-transporting material (HTM) that is crucial for long-term stability. Moreover, even if PSC devices can work without the HTM, this

[a]*LAQV-Requimte and Department of Chemistry, University of Aveiro, 3010-193 Aveiro, Portugal. E-mail: nmoura@ua.pt*
[b]*LEPABE – Laboratory for Process Engineering, Environment, Biotechnology and Energy, Faculty of Engineering, University of Porto, Rua Dr Roberto Frias, 4200-465 Porto, Portugal. E-mail: mafaldapereira@fe.up.pt*
[c]*ALiCE – Associate Laboratory in Chemical Engineering, Faculty of Engineering, University of Porto, Rua Dr Roberto Frias, 4200-465 Porto, Portugal*
[d]*i3N, Department of Physics, University of Aveiro, 3810-193 Aveiro, Portugal*
[e]*University of Coimbra, Centro de Química de Coimbra, Department of Chemistry, Coimbra 3004-535, Portugal*

†Electronic supplementary information (ESI) available: Experimental section and characterisation data. See DOI: https://doi.org/10.1039/d3dt00512g

‡These authors contributed equally to this work.

active layer is essential for high performance as it facilitates charge carrier separation and extraction by transporting holes from the perovskite material to the cathode whilst reducing unwanted charge recombination. Currently, typical n–i–p structured PSCs generally use 2,2′,7,7′-tetrakis[*N*,*N*′-di(4-methoxyphenyl)amino]-9,9′-spirobifluorene (spiro-OMeTAD) as the HTM. Nevertheless, spiro-OMeTAD production costs are high due to the laborious and complex multistep synthesis, resulting in a low yield, combined with a complicated purification process. Furthermore, additives and dopants are needed to improve the spiro-OMeTAD hole mobility capacity, and those accelerate perovskite decomposition to cause detrimental effects on the long-term stability of the whole device. Accordingly, tremendous efforts have been devoted to developing alternative HTMs.[6,7] Low-cost carbazole-based molecules, bearing a wide variety of functional groups to fine-tune electronic and optical properties, have attracted much attention due to PSC performances equalising that of spiro-OMeTAD.[8–10] Meanwhile, porphyrins, due to their high thermal stability and efficient light-harvesting throughout a large portion of the solar emission spectrum, easily tailored peripheral and non-peripheral substituents, and tuneable optical and electronic properties, have shown their great potential as HTMs since the pioneering work carried out in 2016.[11,12] In this first literature report, Zn(II) porphyrin–ethynylaniline conjugates as HTMs in PSCs generated a PCE of 16.6%.[13] Later, Chen *et al.* reported the use of Zn(II) and Cu(II) complexes of 5,10,15,20-tetrakis{4-[*N*,*N*-di(4-methoxyphenyl)amino-phenyl]}porphyrin with outstanding thermal and electrochemical stability. Under the same operating conditions, whilst the Zn(II) complex gave rise to a PCE of 17.78%, comparable to the spiro-OMeTAD PCE of 18.59%, the Cu(II) complex contributed only a PCE of 15.36%.[14] In 2018, a PCE of 18.85% resulted from the utilisation of a Zn(II) porphyrin bearing fluorinated triphenylamine substituents as the HTM. In the same study, efficiencies of 17.71% and 16.37% were reported for non-fluorinated versions, and all these outcomes are a consequence of incorporating F substituents in the periphery of the porphyrin core that creates an increase in charge injection/transfer of the devices due to the better-matched HOMO level and improved hole mobility.[15] Besides, Chiang *et al.* combined triple cation perovskites with porphyrin dimers incorporating ethynylaniline moieties to achieve a PCE of 19.44%, outperforming the widely used spiro-OMeTAD (18.62%).[16] In a broader context, it has been proven that triarylamine substituents in the porphyrin cores have a deep impact on energy levels to play an important role in enhancing charge transport in the amorphous HTM film and thus in improving the PSC device performance. However, there are no reports on the effects of directly *N*-linking *N*-donors to the porphyrin core in the field of HTMs, apart from the work conducted by Cho *et al.* describing Zn(II)-phthalocyanines substituted with secondary amine donor groups, including diphenylamine and carbazole derivatives, as a mixture of positional isomers reaching a maximum PCE of 11.75% for the diphenylamino-substituted macrocycle *vs.* a spiro-OMeTAD-based device achieving 16.78%.[17]

According to previous studies, although the amino groups of *meso*-(diarylamino)porphyrins raise the porphyrin HOMO level, electronic perturbation is only moderate since the diarylamino groups twist out of the bulky porphyrin plane, minimising conjugation.[18] We thus inferred that the introduction of bulky and completely planar *N*-electron-donating groups might be more fruitful due to the increased donating ability of the nitrogen lone pair participating in conjugation, together with the increased steric hindrance due to their completely planar configuration. Following this line of reasoning, Cu(II) and Zn(II)-based porphyrins doubly functionalised with carbazole were readily obtained and successfully used as HTMs in PSC devices. In the present study, also contributing to the fundamental understanding, dibrominated precursor structures, as well as *meso*-unsubstituted porphyrins, were used for the same purpose.

2. Experimental details

2.1. Materials

All chemical reagents and solvents employed in the synthetic procedures were of chemical or analytical grade and used without further purification. Preparative thin-layer chromatography was carried out on 20 × 20 cm glass plates coated with silica gel (0.5 mm thick). Column chromatography was carried out using silica gel (63–200 microns). Analytical TLC was carried out on pre-coated sheets with silica gel (0.2 mm thick). Commercial sources are Sigma-Aldrich, Merck, Acros, Fluorochem, Porphyrin-systems, Macherey-Nagel, and PanReac AppliChem. 5,15-Bis(3,5-di-*tert*-butylphenyl)porphyrin **2** and porphyrins **3a** and **3b** and **4a** and **4b** were synthesised under modified conditions reported in the literature.[19–21] Detailed procedures are provided in the ESI.†

2.2. Measurement and characterisation

2.2.1. Structural characterisation. ^{1}H and ^{13}C solution NMR spectra were recorded on Bruker Avance 300 (300.13 and 75.47 MHz, respectively) and 500 (500.13 and 125.76 MHz, respectively) spectrometers. $CDCl_3$ and CD_3OD were used as solvents and tetramethylsilane (TMS) as the internal reference; the chemical shifts are expressed in δ (ppm) and the coupling constants (J) in hertz (Hz). Unequivocal ^{1}H assignments were made using 2D COSY ($^{1}H/^{1}H$), while ^{13}C assignments were made based on 2D HSQC ($^{1}H/^{13}C$) and HMBC (delay for long-range J C/H couplings were optimised for 7 Hz) experiments. ESI mass spectra were recorded on a Micromass Q-Tof 2 spectrometer (Micromass, Manchester, UK) operating in the positive mode. High-resolution mass spectra were recorded on an LTQ Orbitrap XL mass spectrometer (Thermo Fischer Scientific, Bremen, Germany) using $CHCl_3$ as a solvent. The UV-Vis spectra were recorded on a UV-2501PC Shimadzu spectrophotometer using *N*,*N*′-dimethylformamide or chlorobenzene as a solvent. Emission spectra of compounds **5a** and **5b** were recorded on a FLuoroMax Plus spectrofluorometer using a chlorobenzene : acetonitrile 3 : 1 mixture.

2.2.2. Cyclic voltammetry. An Autolab PGSTAT302N potentiostat was used in electrochemical experiments. Voltammograms were recorded using a three-electrode cell arrangement; a polished glassy-carbon (GC) pin (3 mm in diameter) served as a working electrode, a platinum wire as a counter electrode, and the reference electrode was acetonitrile $Ag|Ag^+$. An acetonitrile solution of $AgNO_3$ (0.01 M) with the addition of 0.1 M Bu_4NPF_6 was used in the compartment of the reference electrode. Porphyrin complexes **5a** and **5b** have extremely low solubility in acetonitrile. For this reason, the solvent mixture chlorobenzene : acetonitrile in a 3 : 1 volume ratio was used for electrochemical studies. The concentration of **5a**, **5b**, and conventional spiro-OMeTAD was 1.9 mM; all solutions contained the Bu_4NPF_6 salt as a supporting electrolyte at a concentration of 0.075 M. Prior to measurements, the solutions were deaerated by purging high purity Ar for *ca.* 5 min. Voltammograms were recorded at a potential scan rate of 100 mV s^{-1}. During the measurement, the Ar flow was kept above the solution in the cell. Electrode potentials in voltammograms are quoted with regard to the equilibrium potential ($E_{1/2}$) of the Fc^+/Fc redox couple in the same mixture of solvents with 0.075 M Bu_4NPF_6 as the supporting electrolyte.

Steady cyclic voltammograms of the GC electrode in Fc solutions, either in acetonitrile or in a mixture of solvents, are presented in the ESI in Fig. S1.† $E_{1/2}$ of the Fc^+/Fc couple for each solvent was defined as the midpoint between potentials corresponding to the oxidation and reduction peaks.

The HOMO energy levels were estimated from the onset potentials of oxidation ($E_{on\ Ox}$) using the equation

$$E_{HOMO}\ (eV) = -(5.1 + *E_{on\ Ox} + **0.042),$$

where: $*E_{on\ Ox}$ is given *vs.* $E_{1/2}(Fc^+/Fc)$ in a 3 : 1 volume ratio of the chlorobenzene : acetonitrile mixture; **0.042 is the difference between $E_{1/2}$ (Fc^+/Fc) in mixed solvents and in acetonitrile. The difference reflects the solvent effect on the redox potential of the internal reference (Fc^+/Fc) and must be used as a correction factor. The formal potential of the Fc^+/Fc redox couple of −5.1 eV at the Fermi scale was obtained using the redox potential of ferrocene in pure acetonitrile.[22]

2.2.3. Electronic structure calculations. The initial structures were constructed and then optimised in GAMESS-US (2018.R3)[23] using the B3PW91 hybrid functional[24] with the LANL2DZ[25] basis set and Effective Core Potentials (ECPs) combination. The basis set was obtained from Basis Set Exchange.[26] As the systems have over 100 atoms, ECPs were used to replace the core electrons with an effective potential and accelerate the calculations. Eighteen core electrons were removed for zinc, ten core electrons were removed for copper, and twenty-eight core electrons for bromine due to the use of ECPs. The B3PW91 functional was used as it was shown to have good results in the description of transition metal chemistry.[27] Default values for the convergence in the geometry optimisation were used in all calculations. The Hessian matrix (second-order partial derivatives of energy concerning the cartesian coordinates of all atoms) was calculated on the final geometries and the absence of negative eigenvalues showed that the geometries correspond to minima. The optimised geometries in the xyz format are available at **https://github.com/peabreu/POR-PSK**. To establish the differences between the optimised structures, all geometries that had the same metal atom were superimposed, minimising the root mean square deviation of the coordinates of the central N atoms. This is shown in Fig. S2 in the ESI.† There is almost no difference in structures when the hydrogen atom is replaced by bromine (blue and red structures). The two 3,5-di-*tert*-butylphenyl groups are not perpendicular to the macrocycle and have a similar angle value (ranging between 50 and 53 degrees) in all structures. Structures **3** and **4** have an almost planar macrocycle (with a deviation from planarity of less than 1 degree), but structures **5a** and **5b** are distorted from planarity by almost 10–20 degrees (measured by calculating the dihedral angle starting in the central metal atom, followed by the nitrogen and the next two bonded carbons in the pyrrole ring). The carbazole substituents in structures **5** are also not perpendicular to the macrocycle ring with angles around 56 and 60 degrees for **5a** and **5b**, respectively. This rotation can be attributed to the repulsion of the hydrogen atoms in the phenyl rings, as well as electronic correlation.[28]

2.2.4. Photoluminescence. Room temperature steady-state photoluminescence (PL) and PL excitation (PLE) were performed in a Fluorolog-3 Horiba Scientific set-up with a double additive grating Gemini 180 monochromator (1200 grooves per mm and 2 × 180 mm) in the excitation and a triple grating iHR550 spectrometer in the emission (1200 grooves per mm and 550 mm). This system is equipped with a 450 W Xe lamp as the excitation source.

2.3. Synthesis

2.3.1. Synthesis of [5,15-di(9*H*-carbazol-9-yl)-10,20-bis(3,5-di-*tert*-butylphenyl)porphyrinato]zinc(II) (5a). To a solution of the Zn(II) complex **4a** (12.1 mg, 0.013 mmol) in CH_2Cl_2 (4 mL) triethylamine (2 drops) was added. The mixture was stirred at room temperature for 30 minutes. After this period, the solvents were removed under reduced pressure. Next, carbazole (11.1 mg, 0.067 mmol, 5 equiv.), $PhI(OAc)_2$ (4.3 mg, 0.013 mmol, 1 equiv.), $NaAuCl_4{\cdot}2H_2O$ (7.9 mg, 0.020 mmol, 1.5 equiv.), and CH_2Cl_2 (4 mL) were added. The mixture was stirred at room temperature for 2 h until the TLC control showed the full consumption of the starting material. Then, the reaction mixture was diluted with CH_2Cl_2, and the organic layer after being washed with water was collected and the solvent was removed under reduced pressure. The crude mixture was purified by preparative thin-layer chromatography using CH_2Cl_2/hexane (1 : 1) as the eluent. After crystallisation from CH_2Cl_2/*n*-hexane, compound **5a** was obtained in 51% yield (7.3 mg).

If the solvent removal step was omitted, compound **5a** was obtained in only 16% yield (2.4 mg).

^{1}H NMR (500 MHz, $CDCl_3$): δ 8.88 (4H, d, J = 4.8 Hz, β-H), 8.58 (4H, d, J = 4.8 Hz, β-H), 8.47 (4H, d, J = 8.0 Hz, 1″,8″-H), 8.03 (4H, d, J = 1.5 Hz, 2′,6′-H-Ph), 7.80–7.68 (2H, m, 2H, 4′-H-Ph), 7.46–7.37 (4H, m, 2″,7″-H), 7.41 (4H, t, J = 7.5 Hz, 3″,6″-H), 6.85 (4H, d, J = 8.0 Hz, 4″,5″-H), 1.54 (36H, s, ^{t}Bu-C$\underline{H}_3$)

ppm. ^{13}C NMR (126 MHz, $CDCl_3$): δ 151.4, 150.6, 148.8, 148.6, 140.8, 133.9 (β-C), 129.8 (β-C), 129.5 (2′,6′-C-Ph), 126.4 (3″,6″-CH), 123.5, 122.7, 121.2 (4′-CH-Ph), 120.4 (1″,8″-CH), 120.0 (2″,7″-CH), 113.7, 111.2 (4″,5″-CH), 36.4, 31.7 (^{t}Bu-$\underline{C}H_3$) ppm. UV-Vis (DMF): λ_{max} (log ε) 429.5 (5.34). 559 (4.03), 607.5 (3.65) nm. MS-ESI(+): *m*/*z* 1078.6 $[M]^{+\bullet}$. HRMS-ESI(+): *m*/*z* calc. for 1078.4635 $C_{72}H_{66}N_6Zn$ $[M]^{+\bullet}$ found 1078.4611.

2.3.2. Synthesis of [5,15-di(9*H*-carbazol-9-yl)-10,20-bis(3,5-di-*tert*-butylphenyl)porphyrinato]copper(II) (5b). Derivative **5b** was prepared using the following approaches:

(i) Buchwald–Hartwig coupling: a Schlenk tube was charged with porphyrin **4b** (10.2 mg, 0.011 mmol), carbazole (37.1 mg, 0.22 mmol, 20 equiv.), ^{t}BuONa (75.7 mg, 0.78 mmol, 71 equiv.), 18-crown-6 (0.9 mg, 0.0034 mmol, 0.3 equiv.), $Pd(OAc)_2$ (1 mg, 0.0045 mmol, 0.4 equiv.), and *rac*-BINAP (4.2 mg, 0.0068 mmol, 0.6 equiv.). Next, the vessel was purged with nitrogen and *N*,*N*′-dimethylformamide/toluene (1 : 2) (3 mL) was added. The reaction mixture was stirred at 120 °C for 2 days. The crude mixture was purified by preparative thin-layer chromatography using CH_2Cl_2/hexane (1 : 4) as the eluent. After crystallisation from CH_2Cl_2/*n*-hexane, compound **5b** was isolated in 39% yield (4.7 mg).

(ii) Ullmann coupling: porphyrin **4b** (32 mg, 0.036 mmol) was dissolved in dimethylsulfoxide (1.5 mL) and the resulting mixture was purged with nitrogen for 5 min. Then, carbazole (59.4 mg, 0.36 mmol, 10 equiv.), *N*-phenylbenzohydrazide (3 mg, 0.014 mmol, 0.4 equiv.), CuI (1.4 mg, 0.007 mmol, 0.2 equiv.), and Cs_2CO_3 (46.3 mg, 0.14 mmol, 4 equiv.) were added. The resulting mixture was stirred at 120 °C under a nitrogen atmosphere for 5 days. After reaching room temperature, the reaction mixture was diluted with CH_2Cl_2, washed first with a saturated solution of $NaHCO_3$, and, finally, with distilled water. Then, the organic phase was separated, and the solvent was removed under reduced pressure. The same conditions described in procedure (i) were used to purify the crude mixture and compound **5b** was isolated in 31% yield (12.2 mg).

(iii) Nucleophilic reaction mediated by $PhI(OAc)_2$/$NaAuCl_4{\cdot}2H_2O$: to a solution of porphyrin **4b** (15.4 mg, 0.017 mmol) in CH_2Cl_2 (5 mL) carbazole (14.2 mg, 0.085 mmol, 5 equiv.), $PhI(OAc)_2$ (5.5 mg, 0.017 mmol, 1 equiv.), and $NaAuCl_4{\cdot}2H_2O$ (10.1 mg, 0.025 mmol, 1.5 equiv.) were added. The mixture was stirred at room temperature for 4.5 h until the TLC control showed the full consumption of the starting material. Then, CH_2Cl_2 was added, the reaction mixture was washed with water and extracted with CH_2Cl_2, and the solvent was evaporated under reduced pressure. After purification of the crude mixture as described in procedure (i), compound **5b** was isolated in 11% yield (2 mg).

UV-vis (chlorobenzene): λ_{max} (log ε) 419.5 (4.54), 542.5 (3.58), 575.5 (3.15) nm. MS-ESI(+): *m*/*z* 1077.5 $[M]^{+\bullet}$. HRMS-ESI(+): *m*/*z* calc. for $C_{72}H_{67}CuN_6$ 1078.4718 $[M + H]^+$ found 1078.4668.

2.4. Preparation and characterisation of perovskite solar cells

Triple cation Cs^+/$CH_3NH_3^+$/$CH(NH_2)_2^+$ perovskites made by an anti-solvent dropping method were used to prepare complete devices as described elsewhere.[29,30]

Fluorine-doped tin oxide (FTO) glass substrates (2 mm thickness, TCO-7, 7 Ω per square, Greatcell Solar) were patterned using a VersaLaser (VLS 2.30, Universal Laser Systems) to create a scribing to electrically isolate the photoelectrode from the counter electrode. In the next step, substrates were mechanically cleaned using a 10% Hellmanex (Hellma GmbH) water solution. After rinsing abundantly with distilled water, substrates were sonicated in a potassium hydroxide ethanolic solution and posteriorly in distilled water, for 10 minutes for each step, and then dried at 55 °C for 30 minutes. Before blocking layer deposition, substrates were subjected to additional cleaning by oxygen plasma treatment (Zepto, Diener) for 10 minutes.

A 50–80 nm TiO_2 blocking layer was deposited *via* spray pyrolysis of a precursor solution containing 0.56 M acetylacetone (Sigma-Aldrich) and 0.18 M titanium diisopropoxide bis (acetylacetonate) (Sigma-Aldrich) in 7 mL of anhydrous isopropanol (Sigma-Aldrich). Substrates were preheated at 450 °C before spray application using an atomiser, using air as a carrier gas. The samples were kept for an additional 45 minutes at the same temperature for the formation of the anatase phase and allowed to cool down to room temperature afterwards.

For the application of mesoporous TiO_2, commercial 30 NR-D paste (Dyesol) was diluted in pure ethanol (VWR) (1 : 6 w/w) and spin-coated on the blocking layer at 5000 rpm for 10 seconds with a ramp of 2000 rpm s^{-1} to achieve a 150–200 nm thick mesoporous layer. Samples were then heated at 100 °C for 10 minutes, for pre-drying, and the film was annealed at 500 °C for 30 minutes. After cooling down to 150 °C, the substrates were immediately transferred to a nitrogen atmosphere glove box (MBraun with pressure varying from 2 to 3 mbar), to prevent moisture adsorption, for depositing perovskite films.

The perovskite solution precursor was prepared by dissolving 1.1 M PbI_2 (Sigma-Aldrich), 0.2 M $PbBr_2$ (Sigma-Aldrich), 0.2 M methylammonium bromide (Dyesol), and 1.0 M formamidinium iodide (Dyesol) in 1 mL of a *N*,*N*′-dimethylformamide/dimethylsulfoxide mixture (8 : 2 v/v, both from Sigma-Aldrich,). Then CsI (Sigma-Aldrich), pre-dissolved as a 1.5 M stock solution in dimethylsulfoxide, was added to the mixed perovskite precursor (1 mL, 5 : 95 v/v) to achieve the desired triple cation composition. The perovskite layer was deposited by spin-coating at 1000 rpm for 10 seconds with a ramp of 200 rpm s^{-1}, followed by 30 seconds at 6000 rpm with a ramp of 2000 rpm s^{-1}; 15 seconds before the end of the second step, 100 μL of chlorobenzene was poured onto the spinning substrate, and instantly a brownish colour appeared. Substrates were immediately heated at 100 °C for 40 minutes to anneal and then cooled down for a few minutes to proceed with the deposition of the hole transporting layer.

70 mM spiro-OMeTAD (Chemoborun) or a 10 mM porphyrin solution in chlorobenzene was used as the HTM. Spiro-OMeTAD was doped at a molar ratio of 0.5, 0.03 and 3.3 with lithium bis(trifluoromethylsulphonyl)imide (LiTFSI, Acros Organics), tris(2-(1*H*-pyrazol-1-yl)-4-tris(2-(1*H*-pyrazol-1-yl)-4-*tert*-butylpyridine)cobalt(III)tri[bis(trifluoromethane)sulfoni-

mide] (FK209, Dyesol), and 4-*tert*-butylpyridine (TBP, Sigma-Aldrich), respectively. Both doped and undoped porphyrin-based HTM solutions were considered. The HTM spin-coating on top of the perovskite layer was made at 4000 rpm for 20 seconds with a ramp of 2000 rpm s^{-1}.

Finally, an approximately 60 nm gold electrode was deposited by thermal evaporation (VapourPhase Ω, Oxford Vacuum Science) on top of the hole transporting layer.

The devices were characterised right after their preparation, at room temperature and in ambient air. The solar simulator (Newport – Oriel, LSH-7320) was calibrated using a single Si photodiode (Newport – Oriel, 91 150 V), and an output of 1000 W m^{-2} (with the reference cell held at 25 °C) with Air Mass 1.5 Global (AM 1.5G) spectral filtering equivalent to 1-sun. *I–V* curves were obtained by applying an external potential load and measuring the generated photocurrent using a Zenium (Zahner Elektrik) workstation controlled by the Thales software package (Thales XT 5.1.4). The scan speed and step potential used were 10 mV s^{-1} and 10 mV, respectively; the individual cells were characterised in the reverse mode (from open-circuit to short-circuit) with a black mask with an aperture of 0.196 cm^2.

3. Results and discussion

3.1. Synthesis

The synthetic strategy to obtain new Zn(II)- and Cu(II)-based porphyrin complexes doubly functionalised with carbazoles **5a** and **5b** is outlined in Schemes 1 and 2, and it required the previous preparation of starting *meso*-dibrominated scaffolds **4a** and **4b** from 5,15-bis(3,5-di-*tert*-butylphenyl)porphyrin **2**. As shown in Scheme 1, porphyrin **2** was obtained in 64% yield by reacting dipyrromethane **1** with 3,5-di-*tert*-butylbenzaldehyde in the presence of catalytic amounts of trifluoroacetic acid (TFA), followed by oxidation with 2,3-dichloro-5,6-dicyano-1,4-benzoquinone (DDQ).[19] Afterwards, metalation of the porphyrin inner core with zinc(II) or copper(II) acetate,[20] followed by bromination of both free *meso*-positions present in complexes **3a** or **3b** with *N*-bromosuccinimide (NBS),[21] afforded the required derivatives **4a** and **4b** in 82% and 85% yields, respectively.

The best protocol to obtain the Zn(II) complex **5a** was based on the nucleophilic substitution reaction involving **4a** and carbazole mediated by $PhI(OAc)_2/NaAuCl_4{\cdot}2H_2O$[31] (Scheme 2). This approach was considered after finding that the reaction of the Zn(II) complex **4a** with the carbazole using either an Ullmann protocol[32] or a Buchwald–Hartwig[33] approach led mainly to the exchange of the metal at the inner core by the catalyst metal [Cu(II) or Pd(II)]. To overcome this issue, the coupling of the carbazole with the Ni(II) complex of 5,15-dibromo-10,20-bis(3,5-di-*tert*-butylphenyl)porphyrin was also performed under Ullmann conditions to afford the desired Ni(II) derivative bearing two carbazole units in 50% yield. However, all subsequent attempts to remove Ni(II) under different acidic conditions, and then to introduce a Zn(II) or Cu(II) ion, led to degradation of the porphyrin and made this approach impractical. In contrast, when the double nucleophilic substitution of **4a** with a carbazole (5 equiv.) was carried out in the presence of $PhI(OAc)_2$ (1 equiv.) and $NaAuCl_4{\cdot}2H_2O$ (1.5 equiv.) in CH_2Cl_2 at room temperature, the desired product **5a** was isolated in 22% yield accompanied by the corresponding free-base in analogous amounts. Further metalation of the free-base with $Zn(AcO)_2$ allowed to isolate **5a** in a total yield of 59%.

To overcome this entire demetallation/metalation process and build up a straight synthetic route, treatment of the dibrominated porphyrin **4a** dissolved in CH_2Cl_2 with triethylamine

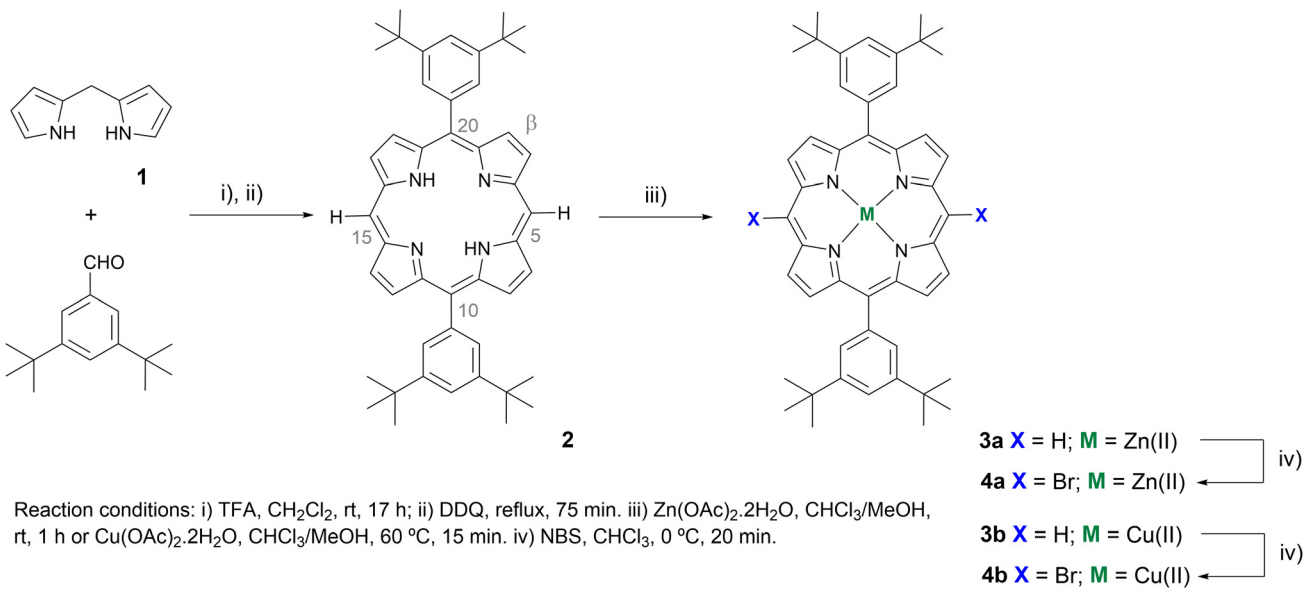

Reaction conditions: i) TFA, CH_2Cl_2, rt, 17 h; ii) DDQ, reflux, 75 min. iii) $Zn(OAc)_2.2H_2O$, $CHCl_3$/MeOH, rt, 1 h or $Cu(OAc)_2.2H_2O$, $CHCl_3$/MeOH, 60 °C, 15 min. iv) NBS, $CHCl_3$, 0 °C, 20 min.

Scheme 1 Synthesis of scaffolds **2–4**.

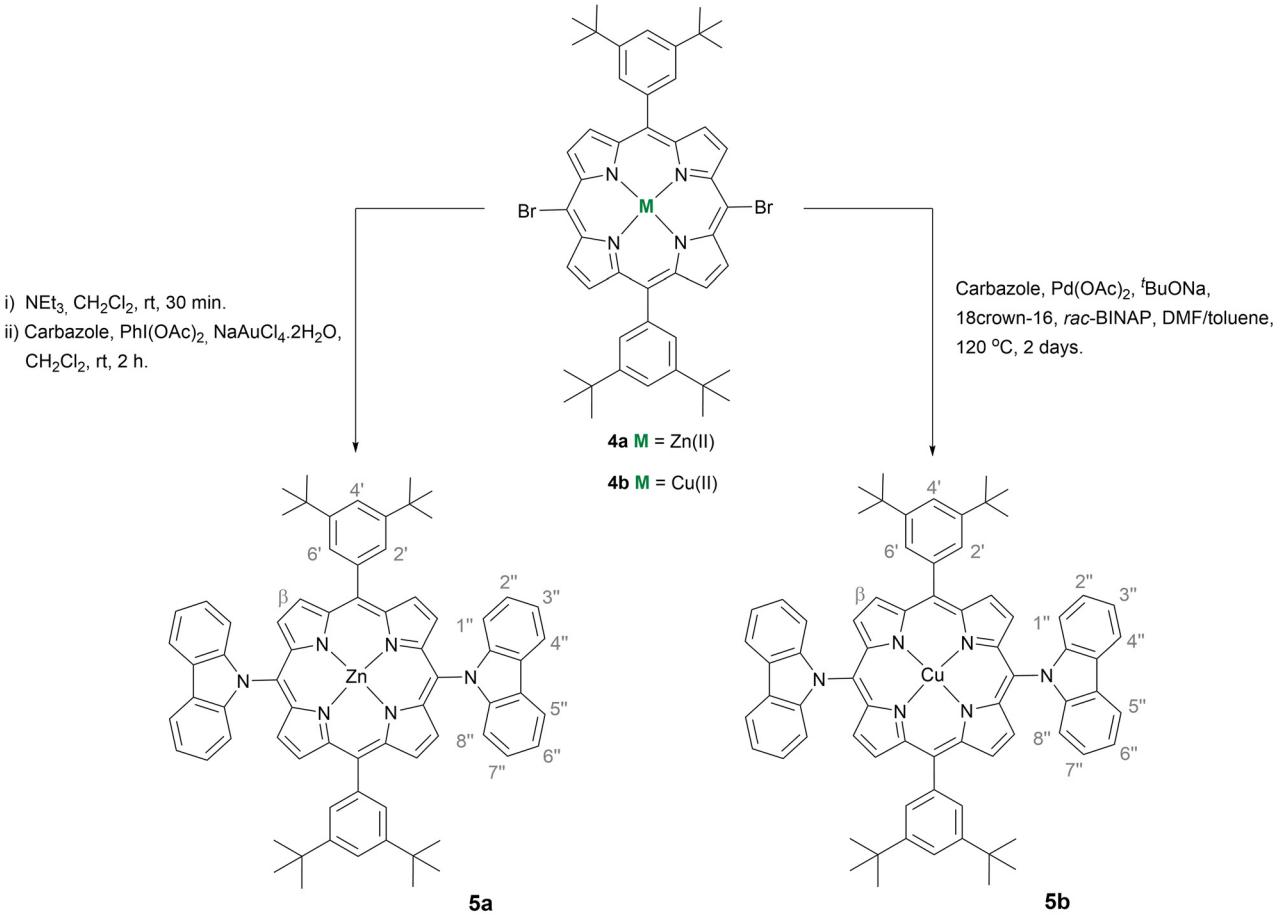

Scheme 2 Synthesis of Zn(II) and Cu(II)-based porphyrin complexes doubly functionalised with carbazoles **5a** and **5b**.

followed by solvent removal was carried out before the oxidative nucleophilic substitution step. Compound **5a** was then isolated in an overall yield of 51%.

When the nucleophilic substitution approach was extended to the Cu(II) complex **4b**, the desired derivative **5b** was just obtained in 11% yield. However, as the exchange of the Cu (II) ion is less probable due to the higher stability of the porphyrinic complex **4b**, the aforementioned Ullmann and Buchwald–Hartwig cross-couplings were again considered (see Table S1†). Under Ullmann conditions, the coupling of **4b** with carbazole (10 equiv.) in the presence of *N*-phenylbenzohydrazide (0.4 equiv.), CuI (0.2 equiv.), and Cs_2CO_3 (4 equiv.) was carried out in dimethylsulfoxide (DMSO) at 120 °C for 5 days to afford the desired derivative **5b** in 31% yield. Considering the Buchwald conditions [carbazole (20 equiv.), $Pd(OAc)_2$ (0.4 equiv.), ^{t}BuONa (71 equiv.), 18-crown-6 (0.3 equiv.), and *rac*-BINAP (0.6 equiv.), at 120 °C in a mixture of *N*,*N*′-dimethylformamide and toluene (1 : 2)], the yield of **5b** was improved to 39% with the reaction time reduced to 2 days. It is worth referring that the desired product was not obtained when the reaction was carried out in tetrahydrofuran; the most common solvents referred to in couplings involve porphyrins.[33b,34]

3.2. Structural characterisation

Structural elucidation of the free-base scaffold **2** and all the Zn(II) complexes described above involved the use of 1D (^{1}H and ^{13}C) and 2D [(^{1}H,^{1}H) COSY, NOESY, (^{1}H,^{13}C) HSQC, and (^{1}H,^{13}C) HMBC] NMR techniques (Fig. S3, S5, S10, and S14–S18†). The ^{1}H-NMR spectrum of the Zn(II) complex **3a**, when compared to compound **2**, showed the absence of the signal corresponding to the resonance of the inner core *N*H protons (δ −3.02 ppm). No noticeable change was observed for the resonances of the remaining protons. In **4a**, the absence of the singlet at δ 10.3 ppm corresponding to the resonance of the protons at *meso*-positions confirmed the success of the dibromination step. When compared to the precursor, the presence of the two bromine atoms induced a deshielding of the doublet generated by the resonances of four β-pyrrolic protons from δ 9.46 to 9.62 ppm, whilst the remaining signals were slightly shifted to the high field.

After the introduction of the carbazole moieties, compound **5a**, the two doublets generated by the resonances of the β-pyrrolic protons were shielded from δ 9.62 and 8.88 ppm to δ 8.88 and 8.58 ppm, respectively. In the aromatic region, four signals appeared ranging from *ca.* δ 8.5 ppm to *ca.* δ 6.8 ppm and correspond to the resonance of the carbazole protons.

The singlet due to the resonances of the methyl protons from the 3,5-di-*tert*-butylphenyl substituents remained almost unchanged, exhibiting a chemical shift around δ 1.5 ppm.

The structures of all Zn(II) and Cu(II) porphyrin complexes were also supported by mass spectrometry (MS-ESI/HRMS-ESI) and UV-Vis spectroscopy. Apart from compound **4b**, which displayed the *m*/*z* signal corresponding to the $[M + 2H]^{+\bullet}$ ion, all the remaining compounds showed the presence of the peak with *m*/*z* corresponding to the $[M]^{+\bullet}$ or $[M + H]^{+}$ ion (Fig. S4, S6–S9, S11–S13, and S19–S22†). As expected, both Zn(II) and Cu(II) porphyrin complexes **3a** and **3b** exhibited typical absorption features of metallo complexes of arylporphyrins with a Soret band assigned to allowed $S_0 \rightarrow S_2$ transitions and two Q bands due to $S_0 \rightarrow S_1$ transitions (Fig. S23†).[35] Bromination of the *meso*-positions induced a red-shift (*ca.* 18 nm) of the Soret band (compounds **4a** and **4b**), while a slight blue-shift (*ca.* 4 nm) was observed after their replacement by carbazole moieties (compounds **5a** and **5b**). Also, in the Q band region, significant changes were observed after the bromination by a red-shift ranging from 20 to 27 nm, and a less noticeable blue-shift after insertion of the carbazole units (3 to 11 nm). Spin-coated films of **5a** and **5b** on glass substrates exhibited similar absorption spectra to those in solution with a slight blue-shift of the Soret and Q bands (*ca*. 10 nm) for Zn(II) complex **5a** relatively to complex **5b** (Fig. S24†).

3.3. Photovoltaic performance

To assess the performance of the synthesised porphyrins as HTMs, n–i–p PSCs were fabricated. A triple cation Cs^{+}/$CH_3NH_3^{+}$/$CH(NH_2)_2^{+}$ perovskite was applied onto a TiO_2 mesoporous layer on top of an electron extraction layer.[29] The porphyrin was then applied as the HTM, over the perovskite layer, and, finally, a thin gold film was deposited to serve as a counter-electrode. For comparison purposes reference cells made of spiro-OMeTAD were used. Lithium bis(trifluoromethylsulphonyl)imide (LiTFSI), tris(2-(1*H*-pyrazol-1-yl)-4-*tert*-butylpyridine)cobalt(III) tri[bis(trifluoromethane)sulfonimide] (FK209) dopants and the 4-*tert*-butylpyridine (TBP) additive were tested to improve the electric conductivity of the HTM layer, either based on the prepared porphyrins or spiro-OMeTAD.

The reference cell, loaded with a HTM layer of spiro-OMeTAD doped with composition A – see Table 1, displayed a typical PCE value of 14.74%, with a short-circuit current density (J_{sc}) of 20.08 mA cm^{-2}, an open-circuit voltage (V_{oc}) of 1.00 V, and a fill factor (FF) of 0.72. It is widely accepted that by reducing Co(III) – present in FK209 – to Co(II), spiro-OMeTAD becomes partially oxidised, rendering the HTM layer more electrically conductive. A cell without FK209 (composition B) displayed a FF of 0.58 and a PCE of 6.01%, similar to the performance of an additive-free cell (composition C), but a much lower J_{sc} of only 7.90 mA cm^{-2}. To further increase the electrical conductivity of the HTM layer, the hygroscopic co-dopant LiTFSI can be added. Indeed, in the absence of LiTFSI, the devices showed much lower photovoltaic parameters and a PCE < 4% (composition D). However, due to the hygroscopic nature of this additive, the stability of as-prepared cells can also be compromised by water absorption during their preparation and under operation.[6,7]

Table 1 Study of the conditions for the preparation of the HTM precursor solutions and photovoltaic characteristics obtained for PSC devices employing standard spiro-OMeTAD and porphyrin **3b** as the hole-transporting layer

HTM	Composition[a]	J_{sc} (mA cm^{-2})	V_{oc} (V)	FF	PCE (%)
spiro-OMeTAD	A	20.8	1.00	0.72	14.71
	B	7.90	0.97	0.58	6.01
	C	13.16	0.78	0.59	6.14
	D	7.51	0.81	0.54	3.33
3b	A	10.09	0.85	0.62	5.30
	B	10.45	0.79	0.51	4.26
	C	5.39	0.76	0.56	2.30

[a] A: 0.5 equiv. of LiTFSI, 0.03 equiv. of FK209, and 3.3 equiv. of TBP per mol of HTM; B: 0.5 equiv. of LiTFSI and 3.3 equiv. of TBP per mol of HTM; C: no additives were used; D: 0.03 equiv. of FK209 and 3.3 equiv. of TBP per mol of HTM.

The role of the HTM additives was also assessed for devices loaded with the *meso*-unsubstituted Cu(II) porphyrin complex **3b** (Table 1). When the **3b** HTM was applied without any dopant, the PCE of the corresponding device remained low, with a value of 2.30%. However, when 0.5 equiv. of LiTFSI with 0.05 equiv. of FK209 and 3.3 equiv. of TBP per mol of HTM was added – optimised composition, the PCE increased to 5.30%. In contrast, the absence of FK209 led to devices with a PCE of 4.26%. It is worth noting that the 10,20-unsubstituted porphyrinic system was selected to eliminate any effect of the substituents at this stage. Subsequently, under this optimised additive composition, the role of the Zn(II) complex **3a** and also the corresponding Ni(II) and Pd(II) complexes were evaluated (Table S2 in the ESI†). It was found that **3a** gave rise to a slightly higher PCE of 6.39%, whilst Ni(II) and Pd(II) complexes resulted in devices with a low PCE of <3%. The last result can be assigned to a poor alignment of the HTM HOMO level with the valence band of the perovskite layer, compared with Cu(II)- and Zn(II)-based porphyrinic HTMs.[14,36]

The study proceeded then to Zn(II) and Cu(II)-based porphyrins **5a** and **5b** doubly functionalised with the carbazole. To the best of our knowledge, no C–N direct bond design in porphyrins has been previously reported as HTMs for PSCs. Only, Pozzi and Nazeeruddin described a Zn(II)-phthalocyanine as a mixture of positional isomers reaching a PCE of 6.65% (*vs.* a spiro-OMeTAD-based device achieving 16.78%).[17]

The feasibility of hole extraction of **5a** and **5b** was evaluated using cyclic voltammetry (CV) – Fig. 1. The HOMO energy levels were estimated from the onset potential of oxidation ($E_{on\ Ox}$), assuming the formal potential of the Fc^{+}/Fc redox couple as −5.1 eV on the Fermi scale.[22] The LUMO was obtained by adding $E_{0\text{–}0} = 1240/\lambda_{int}$ (determined from the interception of the normalised absorption and emission spectra, see Fig. S25†). The obtained data are presented in Table 2, together with the HOMO level of spiro-OMeTAD also

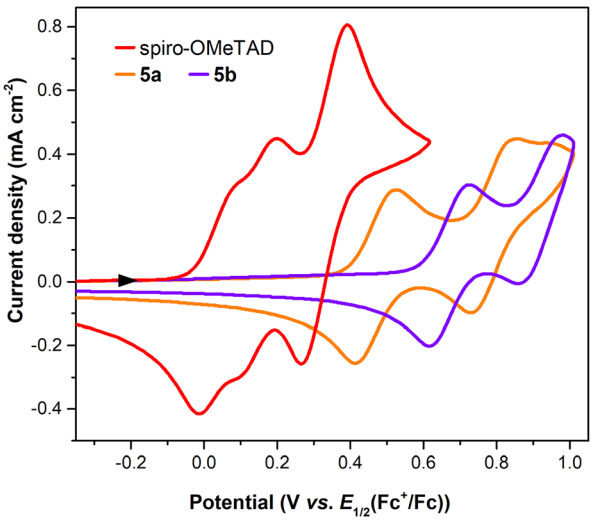

Fig. 1 Cyclic voltammograms obtained on a GC electrode in a 3 : 1 volume ratio of a chlorobenzene : acetonitrile mixture of spiro-OMeTAD and porphyrins **5a** and **5b**.

Table 2 Electrochemistry, photophysics, and HOMO/LUMO levels of HTM materials: spiro-OMeTAD and porphyrins **5a** and **5b**

HTM	$E_{on\ Ox}$ (V)	λ_{int} [a] (nm)	E_{0-0} [b]	E_{HOMO} [c] (eV)	E_{LUMO} [d] (eV)
spiro-OMeTAD	−0.33	n.d.	n.d.	−5.11	−2.50[e]
5a	+0.39	574.7	2.16	−5.54	−3.38
5b	+0.60	585.9	2.12	−5.74	3.62

[a] Determined from the interception of the normalised absorption and emission spectra in a 3 : 1 volume ratio of the chlorobenzene : acetonitrile mixture. [b] $E_{0-0} = 1240/\lambda_{int}$. [c] $E_{HOMO} = -(5.1 + E_{on\ Ox} + 0.042)$. [d] $E_{LUMO} = E_{HOMO} + E_{0-0}$. [e] The E_{LUMO} from spiro-OMeTAD is described in the literature.[38]

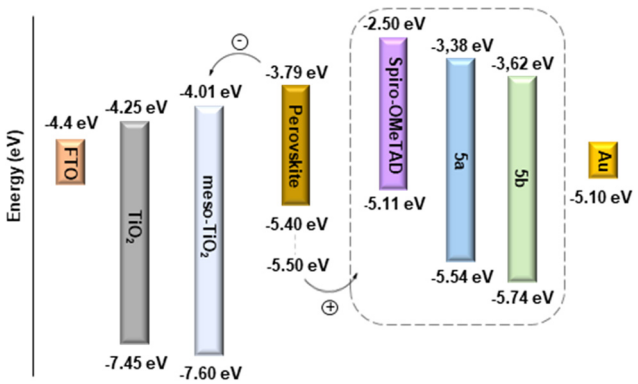

Fig. 2 Energy-level diagram of spiro-OMeTAD and porphyrins **5a** and **5b** in PSC devices.

determined experimentally. As shown in Fig. 2, the HOMO level of spiro-OMeTAD, −5.11 eV, and of the Zn(II) complex **5a**, −5.54 eV, have favourable energy alignment with the perovskite layer (ranging from −5.40 eV to −5.50 eV)[37] and is expected to lead to higher V_{oc} and J_{sc}. The deeper HOMO level of the Cu(II) complex **5b**, −5.74 eV, must hinder the transportation of holes, leading to lower efficiencies. At the same time, the LUMO levels of both **5a** (−3.38 eV) and **5b** (−3.62 eV) are higher than that of the perovskite (−3.8 eV), which must block the electron transport to the Au counter-electrode, hence suppressing the carrier recombination.

The optimised geometry and molecular orbitals of **5a** and **5b** using the B3PW91/LANDL2DZ level of theory are shown in Fig. 3 and also indicate the higher potential of the Zn(II) complex as the HTM. For this complex the HOMO electron density distribution is mainly localised at the porphyrin core and at the twisted carbazole units, while for the Cu(II) complex **5b** it is mainly delocalised over the whole molecule.

The performance of porphyrins **5a** and **5b** as HTMs was evaluated under the optimised conditions previously established for the *meso*-unsubstituted complexes **3**. Fig. 4 shows the current density–potential difference (*J*–*V*) curves of devices with **5a** and **5b** HTMs; the corresponding photovoltaic characteristics are presented in Table 3. As expected, this strong

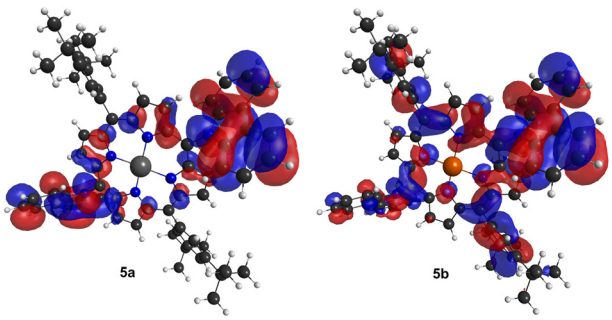

Fig. 3 Density of HOMO frontier molecular orbitals for the optimised geometries of porphyrins **5a** and **5b**. The represented isosurface has a value of 0.0148.

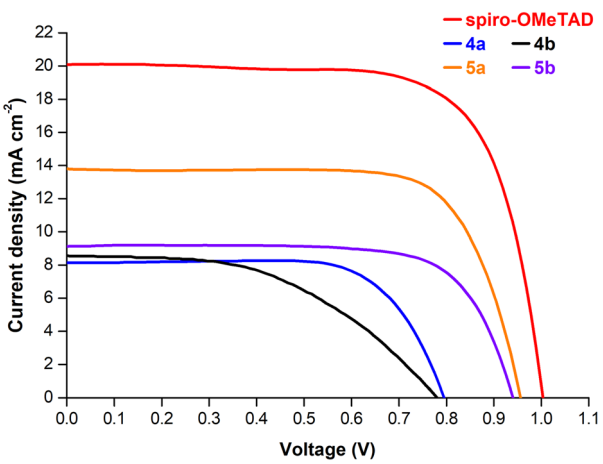

Fig. 4 *J*–*V* curves under simulated 1-sun illumination (AM1.5G) of perovskite solar cells using spiro-OMeTAD and porphyrins **4a**, **4b**, **5a**, and **5b** as the hole-transporting layer.

Table 3 Photovoltaic characteristics obtained for PSC devices employing porphyrins **4a**, **4b**, **5a**, and **5b** as the hole-transporting layer[a]

HTM	J_{sc} (mA cm^{-2})	V_{oc} (V)	FF	PCE (%)
4a	8.15	0.79	0.71	4.68
4b	8.58	0.77	0.49	3.31
5a	13.79	0.96	0.73	9.87
5b	9.14	0.94	0.73	6.37

[a] The HTM precursor solution was prepared considering 0.5 equiv. of LiTFSI, 0.03 equiv. of FK209, and 3.3 equiv. of TBP per mol of HTM.

π-donor group directly connected to the macrocycle produces drastic changes. An improved FF of 0.73 for **5a** and **5b** (*vs.* 0.69 for **3a** and 0.62 for **3b**) and J_{sc} values of 13.79 and 9.14 mA cm^{-2} for **5a** and **5b**, respectively, were recorded. Although significantly lower than those of the spiro-OMeTAD reference cell (*ca.* 14.7%), these devices displayed a PCE of 9.87% for **5a** and 6.37% for **5b**. These photovoltaic performances are substantially higher than those achieved with unsubstituted porphyrins **3a** (PCE = 6.3%) and **3b** (PCE = 5.30%), and higher than Zn(II)-phthalocyanine,[17] pointing out also the critical role of the metallic Zn(II) centre in comparison with Cu(II).

To gain insight into the role of electron-withdrawing substituents in cell performance, dibrominated porphyrins **4a** and **4b** were also used as the HTM layer. Fig. 4 displays the *J*–*V* curves of these devices, whilst the respective photovoltaic characteristics are shown in Table 3. A PCE of 4.68% and 3.31% was obtained respectively for devices based on **4a** and **4b**, which are much lower compared to **5a** and **5b**. In general, halogens, due to their relatively large size, can induce a conformational distortion of the porphyrin core when compared to those caused by other substituent groups.[39] However, the superimposed geometries of **3** and **4** indicate almost no difference in the structures when the hydrogen atom is replaced by bromine (Fig. S2†). This points out that the inductive electron-withdrawing character of the bromine atoms has an important contribution to the lower V_{oc} and J_{sc} values observed for these devices.

To assess the reproducibility of device performance, a batch of 12 individual cells using the Zn(II) porphyrin complexes **3a**, **4a**, and **5a** as HTMs were fabricated (*cf.* Tables S2–S6 in the ESI†). Fig. 5 shows the statistical data for J_{sc}, V_{oc}, FF, and PCE, respectively, along with the spiro-OMeTAD reference (*vide* Table S3†). The performance of prepared devices follows the sequence **4a** < **3a** < **5a** for all parameters except for the FF, where **3a** HTM-based devices display the lowest value. This was assigned to the high solubility of the perovskite in most solvents, and only a few non-polar solvents could be used in HTM deposition, such as benzene (highly toxic), chlorobenzene, or toluene. Porphyrin **3a** is highly soluble in *N*,*N*′-dimethylformamide, but poorly soluble in chlorobenzene or toluene. Therefore, the spin-coating deposition process results in a more irregular distribution of the HTM layer and less intimate contact with the perovskite, which may explain the lower mean FF value and higher standard deviation compared to

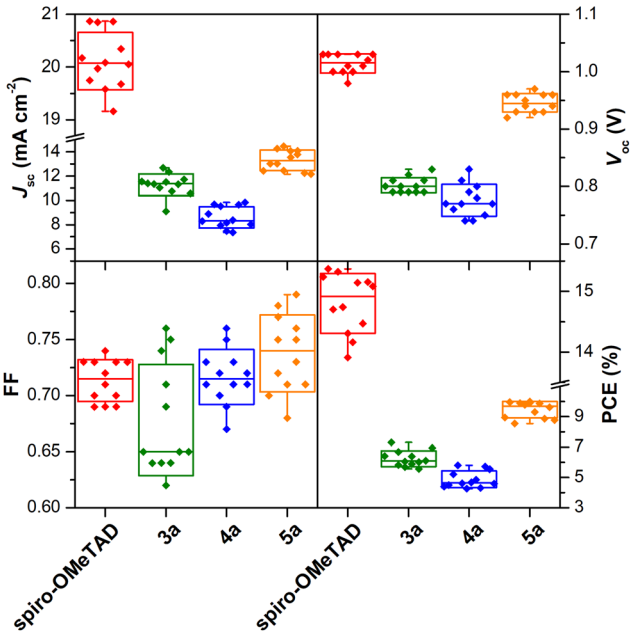

Fig. 5 Statistics of 12 individual PSC devices with the hole-transporting layer made of spiro-OMeTAD and porphyrins **3a**, **4a**, and **5a**.

devices based on **4a** and **5a**. Generally, the **4a** < **3a** < **5a** sequence is fully in line with the evolution of electron-withdrawing substituents – bromine groups, to those with an electron-donor character – carbazole units.

The PCE histograms are plotted in Fig. 6 showing good reproducibility of the PSCs using porphyrin-based HTMs.

Indeed, more than 60% of **5a**-based devices exhibited efficiencies superior to 9.3%, and the best-performing cell reached a PCE of 10.01%, which is 65% of the PCE displayed

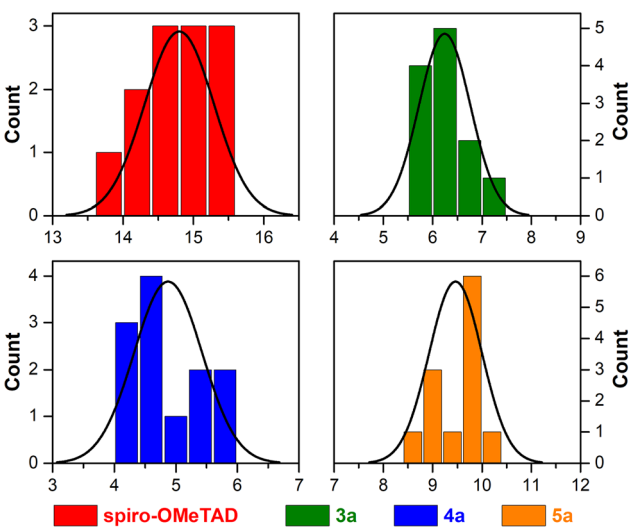

Fig. 6 Histogram data of PCE for 12 individual PSC devices with a hole-transporting layer made of spiro-OMeTAD and porphyrins **3a**, **4a**, and **5a**.

by the spiro-OMETAD reference. Moreover, **5a**-based devices show a remarkably narrower PCE distribution.

These results confirm that the use of porphyrin **5a** provides better performance and, most relevantly, a substantial enhancement in reproducibility, a very relevant characteristic when aiming at the development of devices with potential commercial interest.

3.4. Photoluminescence analysis

To better understand the quality of the perovskite/HTM interface, steady-state photoluminescence (PL) and photoluminescence excitation (PLE) studies were performed. Firstly, the PL emission of the perovskite film on TiO_2/glass substrates was recorded at an excitation wavelength of 550 nm (incidence on the perovskite face), resulting in an emission band with a maximum at *ca.* 755 nm, as can be seen in Fig. 7. PLE recorded at 755 nm evidenced a tail of absorption whose intensity increases from 650 nm up to 500 nm. In addition, its maximum occurs at the same spectral region where porphyrins typically exhibit the maximum absorption (Fig. S24†). So, Zn(II) and Cu(II) porphyrin complexes **5a** and **5b** were also studied when deposited as a film on glass substrates. Fig. 8 shows the results of PL, acquired at two different excitation wavelengths, and PLE experiments performed on **5a** when irradiating at the porphyrin side. The selected excitation wavelengths correspond to a maximum (420 nm) and a minimum (500 nm) of the PLE spectrum. Both PL spectra exhibit two maxima at 621 and 676 nm. Furthermore, the PLE recorded at 676 nm fairly matches the absorption spectrum previously observed in UV-Vis spectra (Fig. S24†). In the case of **5b**, no emission could be detected due to the poor film quality. Hence, for comparison purposes, the powders of both samples were analysed (Fig. S26†). Indeed, both emit within the same spectral region of the PL band of the perovskite, particularly **5b**.

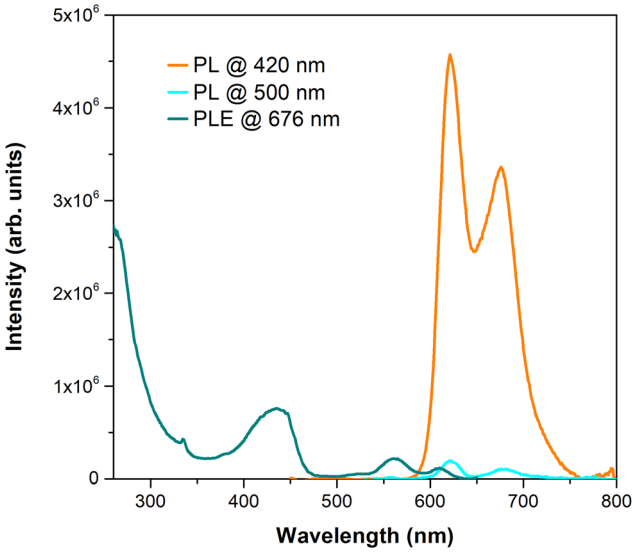

Fig. 8 Photoluminescence spectrum acquired at different excitation wavelengths and photoluminescence excitation spectrum of porphyrin **5a** deposited as a film on a glass substrate (λ_{em} = 676 nm).

Further PL analysis was performed in perovskite-HTM films based on porphyrins **5a** and **5b** and spiro-OMeTAD, as depicted in Fig. 9, to assess the role of the HTM in the perovskite PL recombination. The photoincidence is now placed on the glass surface as for device characterisation. Moreover, in this way, it is ensured that the interfaces are the same either in the absence or the presence of the HTM, minimising possible phenomena related to different light absorption from the HTM layers studied. It was observed that the PL intensity decreased when both porphyrin-based HTMs were used, being

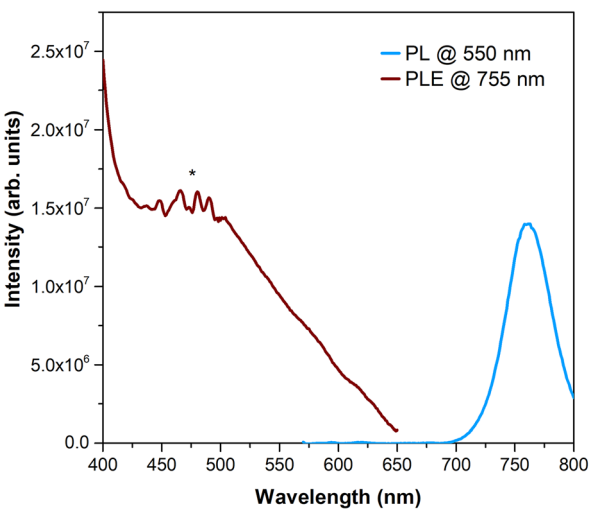

Fig. 7 Room temperature photoluminescence spectrum recorded at 550 nm excitation of a Xe lamp and photoluminescence excitation spectrum of the perovskite monitored at the emission maximum (λ_{em} = 755 nm). *denotes an artefact due to the Xe lamp.

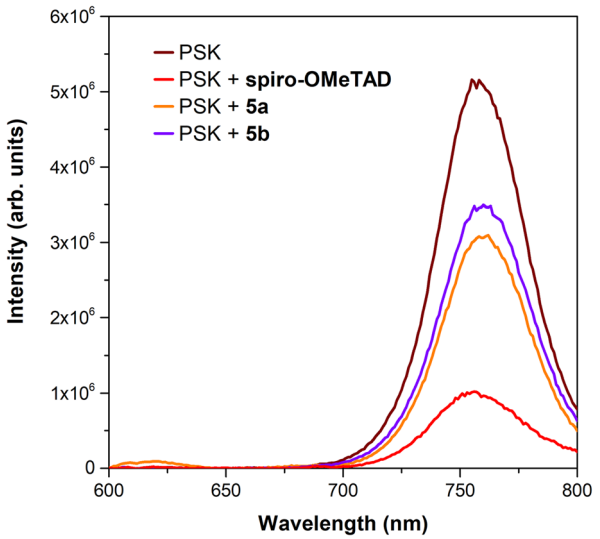

Fig. 9 Photoluminescence spectra acquired at an excitation wavelength of 562 nm of perovskite-HTM films based on spiro-OMeTAD and porphyrins **5a** and **5b**, with the photoincidence placed on the glass substrate.

the higher effect observed for **5a**. However, the strongest decrease was observed for spiro-OMeTAD. A reproducible behaviour was observed regardless of the excitation wavelength used (Fig. S27†), though with distinct relative PL emission intensities. Indeed, this decrease in PL intensity is in good agreement with the behaviour of the *J–V* curves depicted in Fig. 4. These results indicate hole extraction and transfer from the perovskite to the HTM layer, which is in line with the estimated HOMO energy alignment (Fig. 2). Nonetheless, the non-negligible contribution from the porphyrin PL emission can play a role in PL spectra as their emission occurs in the same spectral regions as the perovskite. Accordingly, the contribution of the porphyrin PL signal to the overall spectrum may account for a lower PL intensity reduction when compared to spiro-OMeTAD. Therefore, a direct association between the PL intensity and the charge transfer phenomenon is not straightforward. As a result of this investigation, it becomes evident how important it is to control the optical response of the HTM layer to infer the charge dynamics of hole extraction and transport.

4. Conclusions

A series of Zn(II) and Cu(II)-based porphyrins doubly functionalised with a carbazole were successfully synthesised and used as HTMs in PSC devices. The Cu(II) complex was properly obtained by C–N transition metal-assisted couplings involving the dibrominated porphyrin precursor. Nevertheless, the Zn(II) complex, due to the metal exchangeability and lability behaviour, led to the use of a nucleophilic substitution protocol. Cyclic voltammetry experiments showed the best alignment of the HOMO energy level of the Zn(II) complex **5a** with the perovskite valence band. The optimised geometry and molecular orbitals of both complexes also corroborate the higher potential of **5a** as the HTM. Photoluminescence studies showed emission quenching, compatible with the hole transfer phenomenon. Photovoltaic devices fabricated with a **5a**-based HTM layer displayed a reproducible maximum power conversion efficiency of *ca.* 10%.

These results are the first example of the use of direct C–N linkage involving porphyrins in the preparation of HTMs, and with significantly higher PCEs compared to previously reported devices based on a phthalocyanine analogue, which displayed a PCE of 6.65%. Furthermore, this work highlights the influence of the metal present in the porphyrin cavity, as well as the nature of the substituents on the PCE displayed by the resulting devices.

Author contributions

Melani J. A. Reis: methodology, investigation, formal analysis, and writing – original draft. Ana T. Nogueira: methodology, investigation, and formal analysis. Ana Eulálio: methodology, investigation, formal analysis, and writing – original draft. Nuno M. M. Moura: supervision, conceptualisation, methodology, investigation, formal analysis, and writing – original draft. Joana Rodrigues: methodology, investigation, formal analysis, and writing – original draft. Dzmitry Ivanou: methodology, investigation, formal analysis, and writing – original draft. Paulo E. Abreu: methodology, investigation, formal analysis, and writing – original draft. M. Rosário P. Correia: methodology, investigation, formal analysis, and writing – original draft. Maria G. P. M. S. Neves: supervision, conceptualisation, and writing – original draft. Ana M. V. M. Pereira: funding acquisition, supervision, conceptualisation, methodology, investigation, formal analysis, and writing – original draft. Adélio Mendes: funding acquisition, supervision, conceptualisation, and writing – original draft.

Conflicts of interest

There are no conflicts to declare.

Acknowledgements

The authors thank the University of Aveiro, the University of Porto, and the University of Coimbra. This work was financially supported by UIDB/50006/2020 and UIDP/50006/2020 (LAQV-REQUIMTE), LA/P/0045/2020 (ALiCE), UIDB/00511/2020 and UIDP/00511/2020 (LEPABE), UIDB/50025/2020, UIDP/50025/2020, and LA/P/0037/2020 (i3N), UID/QUI/00313/2020 (Coimbra Chemistry Centre), and Infrastructure Project No. 022161 – the Research Units and Portuguese NMR Network, funded by national funds through FCT/MCTES (PIDDAC); Project FCT POCI-01-0145-FEDER-030357 – "Taylor made porphyrinoids for emerging efficient solar energy devices", funded by FEDER funds through COMPETE2020 – Programa Operacional Competitividade e Internacionalização (POCI) and by national funds (PIDDAC) through FCT/MCTES. M. J. A. Reis (2020.05838.BD), A. T. Nogueira, A. Eulálio, N. M. M. Moura (CDL-CTTRI-048-88-ARH/2018) and A. M. V. M. Pereira thanked FCT and the projects POCI-01-0145-FEDER-030357 and PTD/EQU-EQU/4225/2021 for the research contracts and concession agreements. J. Rodrigues also acknowledges FCT for Programme Stimulus of Scientific Employment – Individual Support (2022.00010.CEECIND).

References

1 J. Nelson, *The Physics of Solar Cells*, Imperial College Press, London, 2003.
2 (*a*) C. Battaglia, A. Cuevas and S. De Wolf, *Energy Environ. Sci.*, 2016, **9**, 1552; (*b*) M. Okil, T. M. Abdolkader and A. Shaker, *Silicon*, 2022, **14**, 1895; (*c*) **https://www.nrel.gov/pv/assets/pdfs/best-research-cell-efficiencies-rev220630.pdf** (accessed June 2023).
3 A. K. Jena, A. Kulkarni and T. Miyasaka, *Chem. Rev.*, 2019, **119**, 3036.

4 J. Y. Kim, J.-W. Lee, H. S. Jung, H. Shin and N.-G. Park, *Chem. Rev.*, 2020, **120**, 7867.
5 A. Kojima, K. Teshima, Y. Shirai and T. Miyasaka, *J. Am. Chem. Soc.*, 2009, **131**, 6050.
6 J. Urieta-Mora, I. García-Benito, A. Molina-Ontoria and N. Martín, *Chem. Soc. Rev.*, 2018, **47**, 8541.
7 G.-W. Kim, H. Choi, M. Kim, J. Lee, S. Y. Son and T. Park, *Adv. Energy Mater.*, 2020, **10**, 1903403.
8 C. Lu, I. T. Choi, J. Kim and H. K. Kim, *J. Mater. Chem. A*, 2017, **5**, 20263.
9 X. Liu, S. Ma, M. Mateen, P. Shi, C. Liu, Y. Ding, M. Cai, M. Guli, M. K. Nazeeruddin and S. Dai, *Sustainable Energy Fuels*, 2020, **4**, 1875.
10 X. Li, N. Sun, Z. Li, J. Chen, Q. Sun, H. Wang and Y. Hao, *New J. Chem.*, 2021, **45**, 735.
11 M. Urbani, G. de la Torre, M. K. Nazeeruddin and T. Torres, *Chem. Soc. Rev.*, 2019, **48**, 2738.
12 Y. Matsuo, K. Ogumi, I. Jeon, H. Wang and T. Nakagawa, *RSC Adv.*, 2020, **10**, 32678.
13 H.-H. Chou, H.-Y. Chiang, M.-H. Li, P.-S. Shen, H.-J. Wei, C.-L. Mai, P. Chen and C.-Y. Yeh, *ACS Energy Lett.*, 2016, **1**, 956.
14 S. Chen, P. Liu, Y. Hua, Y. Li, L. Kloo, X. Wang, B. Ong, W.-K. Wong and X. Zhu, *ACS Appl. Mater. Interfaces*, 2017, **9**, 13231.
15 R. Azmi, U.-H. Lee, F. T. A. Wibowo, S. H. Eom, S. C. Yoon, S.-Y. Jang and I. H. Jung, *ACS Appl. Mater. Interfaces*, 2018, **10**, 35404.
16 Y.-H. Chiang, H.-H. Chou, W.-T. Cheng, Y.-R. Li, C.-Y. Yeh and P. Chen, *ACS Energy Lett.*, 2018, **3**, 1620.
17 K. T. Cho, K. Rakstys, M. Cavazzini, S. Orlandi, G. Pozzi and M. K. Nazeeruddin, *Nano Energy*, 2016, **30**, 853.
18 N. Fukui, W.-Y. Cha, S. Lee, S. Tokuji, D. Kim, H. Yorimitsu and A. Osuka, *Angew. Chem., Int. Ed.*, 2013, **52**, 9728.
19 C. Brückner, J. J. Posakony, C. K. Johnson, R. W. Boyle, B. R. James and D. Dolphin, *J. Porphyrins Phthalocyanines*, 1998, **2**, 455.
20 J. W. Buchler, in *Porphyrins and Metalloporphyrins*, ed. K. M. Smith, Elsevier, Amsterdam, 1975, ch. 5, p. 157.
21 S. G. DiMagno, V. S. Y. Lin and J. M. Therien, *J. Org. Chem.*, 1993, **58**, 5983.
22 C. M. Cardona, W. Li, A. E. Kaifer, D. Stockdale and G. C. Bazan, *Adv. Mater.*, 2011, **23**, 2367.
23 G. M. J. Barca, C. Bertoni, L. Carrington, D. Datta, N. De Silva, J. E. Deustua, D. G. Fedorov, J. R. Gour, A. O. Gunina, E. Guidez, T. Harville, S. Irle, J. Ivanic, K. Kowalski, S. S. Leang, H. Li, W. Li, J. J. Lutz, I. Magoulas, J. Mato, V. Mironov, H. Nakata, B. Q. Pham, P. Piecuch, D. Poole, S. R. Pruitt, A. P. Rendell, L. B. Roskop, K. Ruedenberg, T. Sattasathuchana, M. W. Schmidt, J. Shen, L. Slipchenko, M. Sosonkina, V. Sundriyal, A. Tiwari, J. L. G. Vallejo, B. Westheimer, M. Włoch, P. Xu, F. Zahariev and M. S. Gordon, *J. Chem. Phys.*, 2020, **152**, 154102.
24 A. D. Becke, *J. Chem. Phys.*, 1993, **98**, 5648.
25 P. J. Hay and W. R. Wadt, *J. Chem. Phys.*, 1985, **82**, 299.
26 B. P. Pritchard, D. Altarawy, B. Didier, T. D. Gibson and T. L. Windus, *J. Chem. Inf. Model.*, 2019, **59**, 4814.
27 C. J. Cramer and D. G. Truhlar, *Phys. Chem. Chem. Phys.*, 2009, **11**, 10757.
28 M. Aydin, D. L. Akins, M. Aydin and D. L. Akins, in *Applications of Molecular Spectroscopy to Current Research in the Chemical and Biological Sciences*, IntechOpen, 2016.
29 M. Saliba, T. Matsui, J.-Y. Seo, K. Domanski, J.-P. Correa-Baena, M. K. Nazeeruddin, S. M. Zakeeruddin, W. Tress, A. Abate, A. Hagfeldt and M. Grätzel, *Energy Environ. Sci.*, 2016, **9**, 1989.
30 I. Mesquita, L. Andrade and A. Mendes, *ChemSusChem*, 2019, **12**, 2186.
31 D.-M. Shen, C. Liu, X.-G. Chen and Q.-Y. Chen, *J. Org. Chem.*, 2009, **74**, 206.
32 J. Haumesser, A. M. V. M. Pereira, J.-P. Gisselbrecht, K. Merahi, S. Choua, J. Weiss, J. A. S. Cavaleiro and R. Ruppert, *Org. Lett.*, 2013, **15**, 6282.
33 (*a*) A. M. V. M. Pereira, M. G. P. M. S. Neves, J. A. S. Cavaleiro, C. Jeandon, J.-P. Gisselbrecht, S. Choua and R. Ruppert, *Org. Lett.*, 2011, **13**, 4742; (*b*) A. Nowak-Król and D. T. Gryko, *Org. Lett.*, 2013, **15**, 5618.
34 (*a*) T. Takanami, M. Hayashi, F. Hino and K. Suda, *Tetrahedron Lett.*, 2003, **44**, 7353; (*b*) Y. Chen and X. P. Zhang, *J. Org. Chem.*, 2003, **68**, 4432.
35 M. Gouterman, *J. Mol. Spectrosc.*, 1961, **6**, 138.
36 C.-G. Si, X.-D. Lv and S.-J. Long, *Inorg. Chem. Commun.*, 2020, **112**, 107701.
37 M. Deepa, M. Salado, L. Calio, S. Kazim, S. M. Shivaprasad and S. Ahmad, *Phys. Chem. Chem. Phys.*, 2017, **19**, 4069.
38 L. Nakka, Y. Cheng, A. G. Aberle and F. Lin, *Adv. Energy Sustainability*, 2022, **3**, 2200045.
39 K. J. Flanagan, M. P. Dominguez, Z. Melissari, H.-G. Eckhardt, R. M. Williams, D. Gibbons, C. Prior, G. M. Locke, A. Meindl, A. A. Ryan and M. O. Senge, *J. Org. Chem.*, 2021, **17**, 1149.